A Facet-Specific Quantum Dot Passivation Strategy for Colloid Management and Efficient Infrared Photovoltaics

Younghoon Kim, Fanglin Che, Jea Woong Jo, Jongmin Choi, F. Pelayo García de Arquer, Oleksandr Voznyy, Bin Sun, Junghwan Kim, Min-Jae Choi, Rafael Quintero-Bermudez, Fengjia Fan, Chih Shan Tan, Eva Bladt, Grant Walters, Andrew H. Proppe, Chengqin Zou, Haifeng Yuan, Sara Bals, Johan Hofkens, Maarten B. J. Roeffaers, Sjoerd Hoogland, and Edward H. Sargent*

Colloidal nanocrystals combine size- and facet-dependent properties with solution processing. They offer thus a compelling suite of materials for technological applications. Their size- and facet-tunable features are studied in synthesis; however, to exploit their features in optoelectronic devices, it will be essential to translate control over size and facets from the colloid all the way to the film. Larger-diameter colloidal quantum dots (CQDs) offer the attractive possibility of harvesting infrared (IR) solar energy beyond absorption of silicon photovoltaics. These CQDs exhibit facets (nonpolar (100)) undisplayed in small-diameter CQDs; and the materials chemistry of smaller nanocrystals fails consequently to translate to materials for the short-wavelength IR regime. A new colloidal management strategy targeting the passivation of both (100) and (111) facets is demonstrated using distinct choices of cations and anions. The approach leads to narrow-bandgap CQDs with impressive colloidal stability and photoluminescence quantum yield. Photophysical studies confirm a reduction both in Stokes shift (≈47 meV) and Urbach tail (≈29 meV). This approach provides a ≈50% increase in the power conversion efficiency of IR photovoltaics compared to controls, and a ≈70% external quantum efficiency at their excitonic peak.

Colloidal nanocrystals including metals, semiconductors, and ceramics have been developed through advances in surface and colloid chemistry, and have inspired intense interest in technological applications due to their size-dependent features and their ease of materials processing.[1–10]

The surface structure of colloidal nanocrystals is sensitive to the crystal size. The complex surface structure that emerges immediately following nanocrystal synthesis[11–13] has seen extensive study; but is underexplored in the postsynthetic processes responsible for assembling colloidal nanocrystals into semiconductor thin films.

Lead chalcogenide narrow-bandgap colloidal quantum dots (CQDs) enable harvesting of infrared (IR) light in single- and multijunction thin-film solar cells, since their bandgaps can readily be tuned across the solar spectrum by controlling nanocrystal size.[14–21] Advances

Dr. Y. Kim,[+] Dr. F. Che, Dr. J. W. Jo,[++] Dr. J. Choi,[+++]
Dr. F. P. García de Arquer, Dr. O. Voznyy, Dr. B. Sun, Dr. J. Kim,[++++]
Dr. M.-J. Choi, R. Quintero-Bermudez, Dr. F. Fan, Dr. C. S. Tan, G. Walters,
A. H. Proppe, C. Zou, Dr. H. Yuan, Dr. S. Hoogland, Prof. E. H. Sargent
Department of Electrical and Computer Engineering
University of Toronto
10 King's College Road, Toronto, Ontario M5S 3G4, Canada
E-mail: ted.sargent@utoronto.ca

(iD) The ORCID identification number(s) for the author(s) of this article can be found under https://doi.org/10.1002/adma.201805580.

[+]Present address: Convergence Research Center for Solar Energy, Daegu Gyeongbuk Institute of Science and Technology (DGIST), Daegu 72988, Republic of Korea
[++]Present address: Department of Energy and Materials Engineering, Dongguk University, Seoul 04620, Republic of Korea
[+++]Present address: Department of Energy Science and Engineering, Daegu Gyeongbuk Institute of Science and Technology (DGIST), Daegu 72988, Republic of Korea
[++++]Present address: Photo-electronic Hybrids Research Center, Korea Institute of Science and Technology (KIST), Seoul 02792, Republic of Korea

Dr. E. Bladt, Prof. S. Bals
Electron Microscopy for Materials Science (EMAT)
University of Antwerp
Groenenborgerlaan 171, B-2020 Antwerp, Belgium

Dr. H. Yuan, Prof. J. Hofkens
Departement of Chemistry
KU Leuven
Celestijnenlaan 200F, 3001 Heverlee, Belgium

Prof. M. B. J. Roeffaers
Center for Surface Chemistry and Catalysis
Faculty of Bioscience Engineering
KU Leuven
3001 Heverlee, Belgium

in the surface chemistry of colloidal nanomaterials have enabled significant progress in the synthesis[22–29] and surface modification[30–36] of IR CQDs. Recently, lead halide-based solution-phase ligand exchanges on CQDs having a 1.3 eV (≈950 nm) bandgap resulted in the highest-performing CQD solar cells to date, with certified power conversion efficiencies (PCEs) reaching 12% under simulated AM1.5 full solar illumination.[33,34] These advances were enabled by a careful size control and surface passivation in the solution phase; however, these new strategies have so far failed to translate to IR applications that rely on larger-diameter dots (i.e., >3.5 nm).

As the CQD size increases, the portion of nonpolar (100) facets with low surface energy increases at the expense of cation-rich polar (111) facets.[27,29] Oleic acid is more weakly bound to nonpolar (100) facets compared to (111) facets:[29] indeed it detaches readily from the (100) facet in polar solvents. This property, exploited in large-diameter CQDs to form locally-ordered superstructures via (100) facet assembly,[37–40] produces CQD aggregation during solution-phase colloid management. We posited that this could underlie the failure of the best-performing previously-developed solution-phase ligand exchanges to enable high-quality longer-wavelength semiconductor solids.

We report herein a strategy to preserve colloidal stability and quantum confinement in narrow-bandgap CQDs during the solution-phase ligand exchange. We sought nonpolar (100) facet passivation in large-diameter CQDs by first replacing the ammonium cation (NH_4^+) used in conventional ligand exchange with alkaline metal cations: this enabled much better solubilization of narrow-bandgap CQDs in polar solvents during the ligand exchange.[33,34] In light of the ionic sizes of the alkaline cations, taken together with the dissociation constant of alkaline metal acetate, we focused on sodium acetate ($Na^+ \cdot Ac^-$), which has the appropriate ionic size as well as a high dissociation constant.[41] We hypothesized that this strategy could provide facet-specific passivation via sodium (Na) and lead halides on the (100) and (111) facets of CQDs, respectively. Na-passivation of the (100) facet enables improved colloidal stability for narrow-bandgap CQDs in polar solvents, leading to superior photophysical properties.

The new strategy significantly enhanced solar cell performance, leading to ≈33% and ≈50% increases in PCEs under full and 1100 nm filtered solar spectra respectively, compared to the lead halide-only passivated CQDs fabricated using the conventional ligand exchange method. The best-performing devices showed record-high external quantum yields (EQEs) that reached ≈70% at the excitonic peak.

Schematic illustrations (**Figure 1**a) depict conventional and facet-specific solution ligand exchange for narrow-bandgap CQDs. CQDs with size-tunable bandgaps have a high-symmetry rock-salt structure and, when synthesized as nanocrystals using an oleic acid ligand, exhibit well-defined (111) and (100) facets (Figure S1, Supporting Information).[27,29] The surface of ultrasmall CQDs is dominated by the (111) facet, producing an octahedral nanoparticle shape. The (100) facet is expected to appear gradually with increasing CQD size, altering the (111) facet-only octahedron to the (111)/(100) cuboctahedron shape.[27] As-synthesized CQDs, stabilized by oleic acid ligands on the (100) and (111) facets through different binding mechanisms, are highly dispersible in nonpolar solvents such as octane.[29]

In previously reported processing methods, the ligand exchange of oleic acid to lead halides (i.e., $[PbX_3]^-$) occurs mainly on the Pb-rich and polar (111) facets of CQDs. This leads to a higher affinity of anionic ligand species with the aid of acidic NH_4^+ cations.[33,38] However, this method is not suited for narrow-bandgap CQDs exhibiting a fraction of larger (100) facets. Such CQDs are not colloidally stabilized, and thus aggregate and even fuse during ligand exchange as oleic acid ligands on (100) facets are easily removed in polar solvents such as dimethylformamide (DMF) (Figure 1a,b).[37,40] As a result, ligand-exchanged CQDs of large diameter show a brown turbid color in DMF solvent and a clumped structure: a symptom of degraded colloidal stability (Figure 1b and Figure S2: Supporting Information). This indicates that the unpassivated (100) facets contribute to CQD aggregation, corresponding to reduced colloidal stability in polar solvents. Decreased access to surface sites during the exchange diminishes the extent to which lead halide ligands can be adsorbed onto the (111) facets during the solution-phase ligand exchange.

We targeted passivation of (100) facets to avoid aggregate assembly via unpassivated (100) facets in polar solvents that lead to CQD flocculation. By replacing the $NH_4^+ \cdot Ac^-$ with the $Na^+ \cdot Ac^-$ in a lead halide-based ligand exchange process, we pursued facet-specific passivation of CQDs with Na-passivated (100) facets and lead halide-passivated (111) facets, providing a higher degree of colloidal stability during and after the solution ligand exchange. This results in an increased presence of lead halide ligands on (111) facets due to the significantly reduced degree of aggregation during colloidal processing (Figure 1c). X-ray photoelectron spectroscopy (XPS) confirms that CQD solids prepared from the new passivation scheme exhibit an increased iodine signal associated with the PbI_3^- anion ligands, in addition to the presence of Na. Each observation agrees with the overall evidence of improved passivation, and the higher iodine concentration agrees with the observation of more negative charges on CQD surfaces (Figure 1d and Figures S3 and S4: Supporting Information).

We examined the adsorption strength of Na* and NH$_4$* on a PbS(100) surface using density functional theory (DFT) calculations.[42,43] The differential charge density shows that electron exchange between Na* and PbS(100) is more favorable compared to that between NH$_4$* and PbS(100). This suggests that the adsorption strength of Na* on PbS(100) is stronger than that of NH$_4$* (**Figure 2**a). This corresponds well with adsorption energy (E_{ad}) calculations for Na on PbS(100), which reveal a stronger binding of Na* compared to NH$_4$* (Table S1, Supporting Information). In addition, Na 1s core level binding energy shift (CLBEs) calculations[44] along with experimental XPS results reveal Na$^+$ sits preferentially on PbS(100) surfaces rather than on PbS(111). We found that Na binds to sulfur rather than lead on (100) facets, while in PbS(111), Na-adsorption occurs specifically on (111) facets passivated using iodine species.

The CLBE of Na 1s adsorbed on the iodine-covered (111) surface shifts only over the range of −0.1 to 0.0 eV (with Na coverage: 1/9 monolayer (ML) or 1/3 ML) relative to $Na^+ \cdot Ac^-$ salt reference (Figure 2b and Figure S5: Supporting Information). In contrast, the CLBE of Na 1s on (100) surface shifts over the range of 0.5 to 0.8 eV (with Na coverage: 1 ML to 1/16 ML) (Figure S6, Supporting Information). This is consistent with
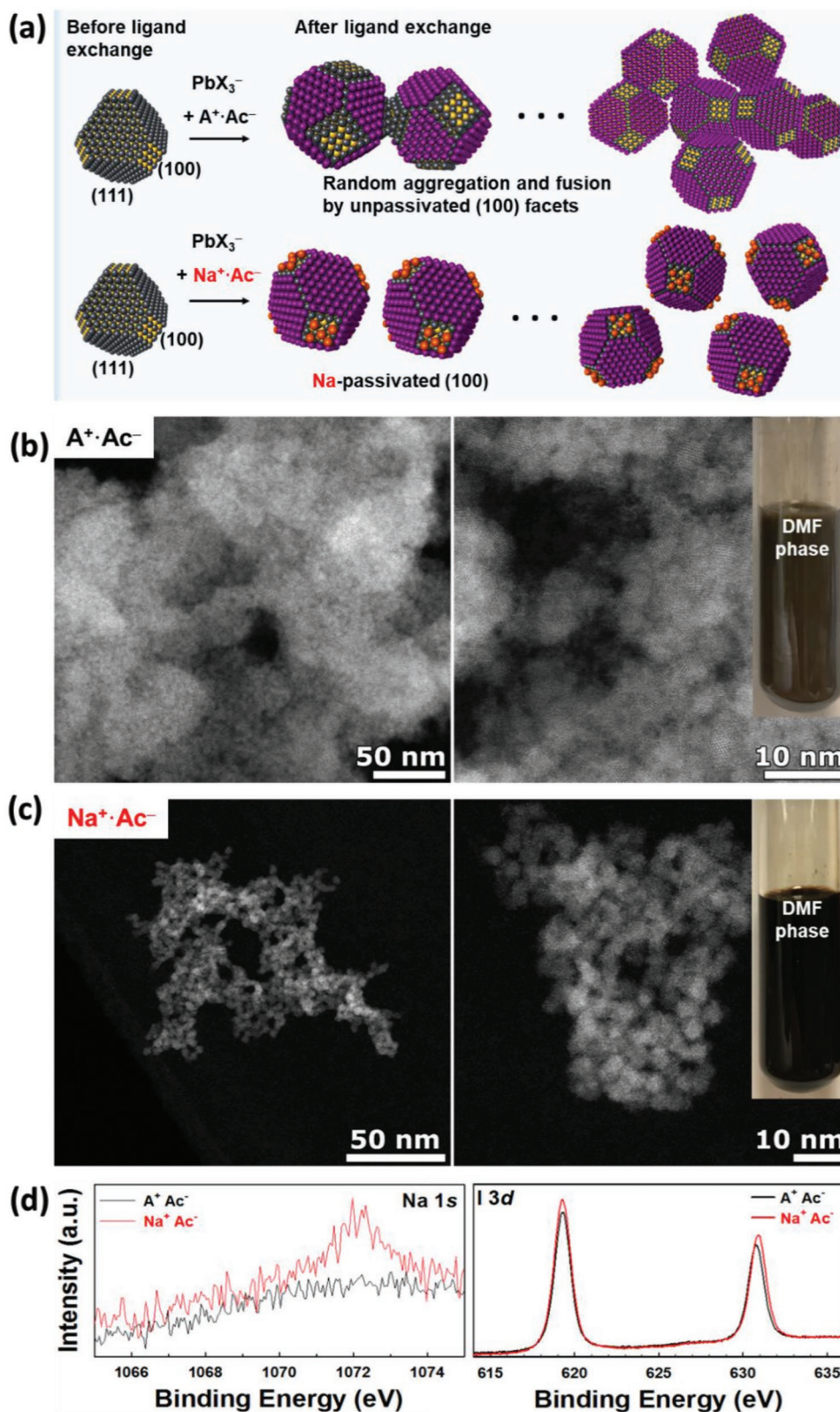
Figure 1. Lead-halide-passivated CQDs with and without Na-passivation on the (100) facets. a) Schematic illustrations of the conventional and facet-specific solution ligand exchanges for narrow-bandgap CQDs. b,c) HAADF-STEM images of ligand-exchanged CQDs using the conventional method (b) and ligand-exchanged CQDs using the facet-specific method (c). The photo images in (b,c) exhibit each CQD solution after solution-phase ligand exchange process. d) XPS results for Na 1s and I 3d peaks of each CQD after ligand exchange in solution phase.
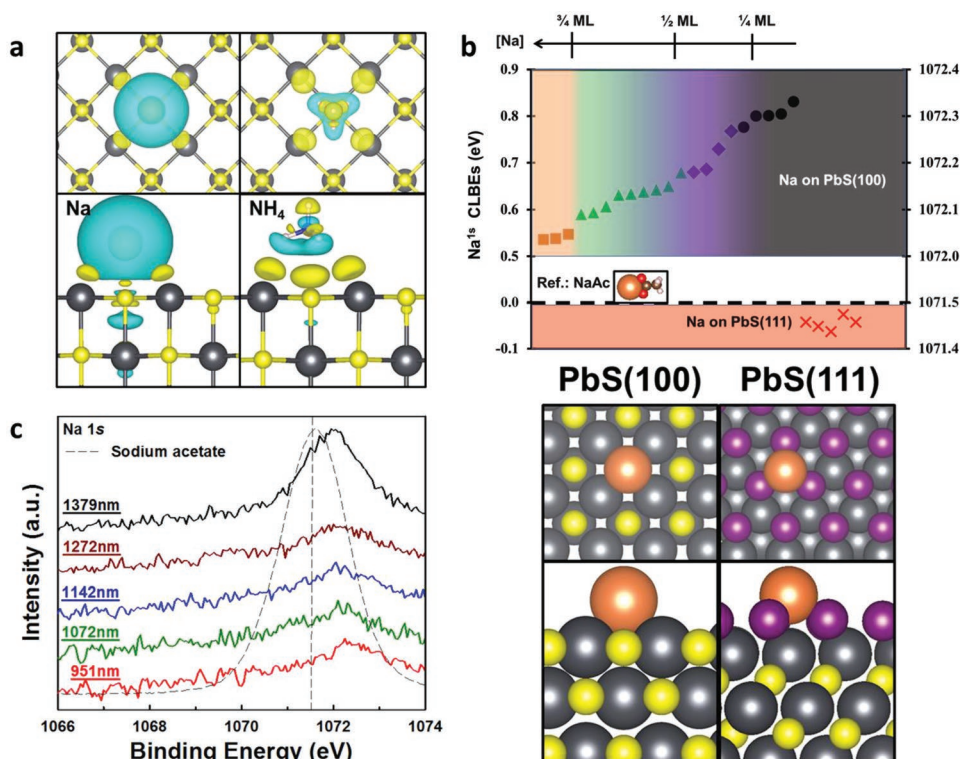
Figure 2. Effects of Na on PbS(100) facets. a) Differential charge densities of Na^+ and NH_4^+ on a PbS(100) surface with the coverage of 1/4 monolayer (ML). The isosurface level of the differential charge densities is 0.001 electrons $bohr^{-3}$, and the yellow or blue areas represent a gain or loss of electron, respectively. The Na, H, N, S, and Pb atoms are represented by the orange, pink, blue, yellow, and gray spheres, respectively. b) The theoretical Na 1s CLBEs for Na adsorbed on PbS(100) and PbS(111) with various Na coverage. All the Na 1s CLBEs referred to the one in $Na^+\cdot Ac^-$. The Na, I, S, and Pb atoms are represented by the orange, pink, yellow, and gray spheres, respectively. c) Na 1s binding energy shift of dually passivated PbS CQDs with different bandgaps measured from XPS, comparing with the Na 1s binding energy of $Na^+\cdot Ac^-$ as a reference.

the Na 1s binding energy shift of Na-passivated CQDs obtained from the XPS measurements, comparing with Na 1s binding energy of $Na^+\cdot Ac^-$ as a reference (Figure 2c). These results indicate that Na is concentrated primarily on the (100) facet. In addition, elemental analysis using inductively coupled plasma atomic emission spectrometry (ICP-AES) reveals that Na remains on the CQDs after ligand exchange (Figure S7, Supporting Information).

This new facet-specific passivation enabled narrow-bandgap CQDs to achieve a high solution-phase photoluminescence quantum yield (PLQY) in DMF (18% PLQY). This is higher than that of lead halide-only exchanged CQDs (1.5% PLQY), and close to the PLQY of original oleic acid-capped CQDs in octane (20% PLQY) (Figure S8, Supporting Information). Absorption and photoluminescence (PL) spectra reveal the effect of facet-specific passivation on the CQD solids, fabricated using the well-dispersed and dually passivated CQDs. These show a narrower exciton peak with a full-width at half-maximum (FWHM) of 84 meV, compared to that of lead halide-only passivated CQDs (94 meV) having the same peak position of 1180 nm. In addition, the PL spectrum shows that the FWHM of dually passivated CQDs (112 meV) is narrower than that of lead halide-only passivated CQDs (133 meV). The blue-shift of PL peak position reveals a smaller Stokes shift of 47 meV for dually passivated CQDs, compared to that of 62 meV for lead halide-only passivated CQDs (**Figure 3**a). This indicates that

the energetic disorder is minimized as a consequence of the significantly reduced degree of CQD aggregation, leading to improved surface passivation.[45,46]

To investigate the effect of energetic disorder in CQD solids in more detail, we examined optical absorption using photothermal deflection spectroscopy. This technique allows investigation of the tail states below the bandgap, allowing estimation of the Urbach energy.[47,48] We found that CQD solids passivated using Na and lead halide showed an Urbach energy of 29 ± 1 meV, which is 40% lower than that of lead halide-only passivated CQD solids (47 ± 2 meV) (Figure 3b).

Transient absorption (TA) spectroscopy revealed that dually-passivated CQDs exhibited a narrower bleach peak compared to lead halide-only passivated CQDs, indicating a reduced polydispersity and lowered energetic disorder (Figure 3c). Gaussians fits of the TA spectra show a narrower FWHM of the excitonic bleaching signal of dually passivated CQDs (29 ± 1 meV) versus lead halide-only (34 ± 3 meV). Dually passivated CQDs exhibit longer lifetimes ($\approx 27 \pm 2$ ns) compared to lead halide-only passivated CQDs ($\approx 19 \pm 1$ ns) (Figure 3d). These photophysical studies indicate that the facet-specific passivation strategy enables reduced energetic disorder (i.e., a flattened energy landscape) of narrow-bandgap CQDs.

Field-effect transistor (FET) measurements revealed that the new protocol provides an approximately fourfold reduction in trap state density when dual passivation is used compared to
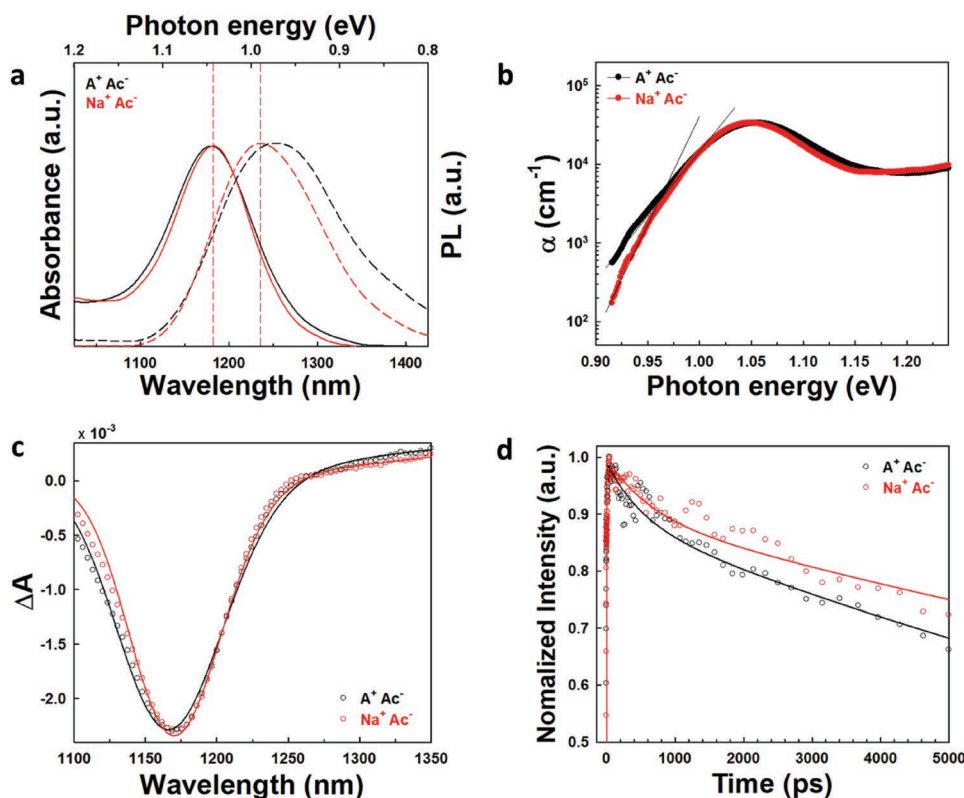
ADVANCED
SCIENCE NEWS

www.advancedsciencenews.com

ADVANCED
MATERIALS

www.advmat.de

Figure 3. Photophysical studies on halide-passivated CQD solids with and without additional Na passivation. a) Absorption and PL spectra of CQD solids prepared using $NH_4^+ \cdot Ac^-$ (black) and $Na^+ \cdot Ac^-$ (red), respectively. b) Photothermal deflection spectroscopy measurements for each sample. The calculated Urbach energy is 28.5 meV for the dually passivated CQD solid using Na and lead halide (red), 46.7 meV for the lead halide-only passivated CQD solid (black). c) Excitonic bleaching peak with Gaussian fitting measured from TA. d) Lifetimes at the central bleach with fits measured from TA.

the case of lead halide-only passivation (Figure S9, Supporting Information).[49] We carried out ultraviolet photoelectron spectra (UPS) measurements in order to investigate the energy band levels. Lead halide-only and dually passivated CQDs showed no shift in the energy levels of conduction and valence bands (Figure S10, Supporting Information).

We then pursued enhanced photovoltaic performance from narrow-bandgap CQDs prepared via the facet-specific passivation strategy. We fabricated solar cell devices using spin-coated layers of lead halide-exchanged CQDs with and without Na-passivation on (100). The device architecture consists of CQD photovoltaic layer deposited onto ZnO-coated indium tin oxide (ITO) electrodes as an electron-transporting layer (ETL) and a thin layer of 1,2-ethanedithiol (EDT)-treated CQDs (EDT-CQDs) as a hole-transporting layer (HTL) and gold deposition as the top metal electrode (**Figure 4**a). Current density–voltage ($J–V$) curves for each device were acquired under AM1.5-simulated full solar illumination (Figure 4b). The photovoltaic parameters of CQD solar cells made using the facet-specific passivation strategy are significantly improved, leading to an 8% increase in open-circuit voltage (V_{OC}), a 7% increase in J_{SC}, a 14% increase in fill factor (FF), and overall a 33% increase in PCE compared to the best-performing CQD solar cells fabricated using conventional lead halide-only passivation.

We measured the solar cell devices under filtered AM1.5 illumination mimicking the effect of absorption by a front wider-bandgap Si solar cells (i.e., beyond 1100 nm). This allowed to examine light-harvesting capability in the IR region unharvested by silicon. The photovoltaic performance of each device after 1100 nm long-pass filter reveals that facet-specific passivation leads to a 13% increase in V_{OC}, a 21% increase in J_{SC}, a 6% increase in FF, and consequently a 48% increase in the PCE of the best-performing devices, compared to the case of lead halide-only passivation (Figure 4c and Figure S11: Supporting Information). Histograms of device performance are shown in Figure S12 in the Supporting Information. Recently it has been reported that IR CQD solar cells fabricated operate efficiently, without need for UV-activation, on improved ZnO ETLs, an advance key to enabling the use of IR CQD solar cells as back cells in front-cell-filtered tandem photovoltaics.[50]

The EQE spectra further confirm the benefits of facet-specific passivation (Figure 4d). A significant EQE increase of dually passivated CQDs beyond 1100 nm with an exciton peak of ≈70% is obtained, corresponding to an expected J_{SC} of 3.1 ± 0.1 mA cm^{-2}. This is in contrast to lead halide-only passivated devices (EQE = 50% and J_{SC} = 2.5 ± 0.1 mA cm^{-2}) (Figure S13, Supporting Information). The expected J_{SC} of lead halide-only and dually passivated CQD solar cell devices are measured to be 23.8 ± 0.6 and 25.7 ± 0.4 mA cm^{-2} for the full solar spectrum, in agreement with measured J_{SC} values under AM1.5.

We also characterized the photovoltaic performance of CQD solar cells based on lead halide-only passivated CQD

**ADVANCED
SCIENCE NEWS**

www.advancedsciencenews.com

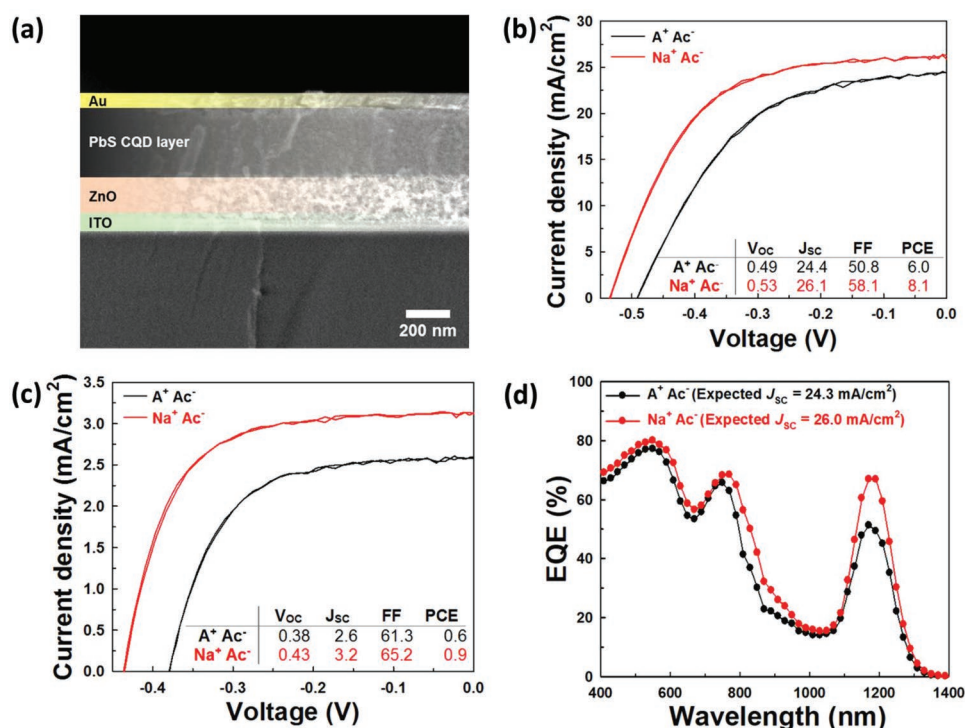**ADVANCED
MATERIALS**

www.advmat.de

Figure 4. Halide-passivated CQD solar cell devices with and without Na-passivation on (100) facets. a) Cross-sectional scanning electron microscopy (SEM) image of an IR CQD solar cell device. b,c) Current–voltage (*J–V*) characteristic of the lead halide-only and dually-passivated CQD solar cells under AM1.5 simulated solar illumination (b), and after using a silicon solar cell representative filter (long-pass 1100 nm filter) (c). d) EQE spectra for each solar cell device measured from 400 to 1400 nm.

inks prepared using different concentrations of $NH_4^+ \cdot Ac^-$ in the ligand exchange solution. As the amount of $NH_4^+ \cdot Ac^-$ increases, narrow-bandgap CQDs show phase-separation during the solution ligand exchange: more NH_4^+ in the polar solvent produces better stabilization of the colloidal phase.[30,33] However, too large an amount of $NH_4^+ \cdot Ac^-$ results in CQD fusion, which we attribute to the effect of NH_4^+ on the surface: the CQDs suffer from the elimination of Pb-oleate from the surface and become fused.[26,51,52] As a result, photovoltaic parameters decrease with increased $NH_4^+ \cdot Ac^-$ for the same thickness of active layer film (Figure S14, Supporting Information). This agrees with the finding that absorption and PL spectra peaks become broader upon CQD fusion (Figures S15 and S16, Supporting Information).

This work demonstrates facet-specific passivation implemented in a solution-phase ligand exchange process, enabling well-passivated and colloidally-stable CQD inks. Na cations selectively passivate nonpolar (100) facets that had previously been left unaddressed, leading to a facet-specific passivation on both polar (111) and nonpolar (100) facets in ligand-exchanged CQDs. The approach enabled protection against CQD aggregation during ligand exchange, improved stability of the exchanged colloid, and enhanced photophysical properties. The dually passivated CQD solids prepared via the facet-specific strategy show improved solar cell performance under AM1.5 full solar spectrum (33% increase in PCE) and beyond 1100 nm (48% increase in PCE), with ≈70% EQE at the excitonic peak. Since the surface structure of colloidal

nanocrystals varies with crystal size, the approach provides a means to achieve further improvements in nanocrystal-based devices.

Experimental Section

Preparation of PbS CQDs: Oleic-acid PbS CQDs (OA-CQDs) were synthesized using a previously published method.[28] Dually passivated PbS CQDs were prepared through a solution ligand exchange process of OA-CQDs in a test tube under atmospheric conditions as follows. First, for precursor solutions, 0.23 mg (0.50 mmol) of lead iodide (PbI_2), 0.037 mg (0.11 mmol) of lead bromide ($PbBr_2$), and 0.017 mg (0.21 mmol) of sodium acetate ($Na^+ \cdot Ac^-$) were completely dissolved in 5 mL of DMF. 5 mL of OA-CQDs dispersed in octane (6 mg mL^{-1}) were added to the precursor solution, and transferred to DMF phase by vortexing vigorously for 5 min. The PbS CQDs in DMF phase were then washed three times using octane in order to remove residual original ligands (i.e., OA). After being washed completely, the dually-passivated PbS CQDs were precipitated by adding toluene (2.5 mL) as an antisolvent, and dried under vacuum for 20 min, and finally dispersed in a mix of 90% butylamine (BTA) and 10% DMF at the desired concentrations. For the lead halide-only passivated PbS CQDs, $Na^+ \cdot Ac^-$ was replaced in the same recipe above mentioned with ammonium acetate. In this case, two phase CQD solution after ligand exchange was not clearly phase-separated, therefore it was forced by centrifugation to separate two phase for removing the remaining OA from DMF phase.

Measurement of High Angle Annular Dark Field Scanning Transmission Electron Microscopy (HAADF-STEM): High resolution HAADF-STEM images were acquired using a cubed FEI Titan microscope operating at 300 kV. A probe semiconvergence angle of ≈20 mrad was used.

**ADVANCED
SCIENCE NEWS**

www.advancedsciencenews.com

**ADVANCED
MATERIALS**

www.advmat.de

Measurement of XPS: XPS measurements were performed using a Thermo Scientific K-Alpha system, with a 50 eV pass energy, and binding energy steps of 0.05 eV. All binding energy values were corrected relative to the reference C 1s peak (284.5 eV). All signals were normalized to Pb.

Measurement of Optical Absorption, PL, and PLQY: The total light absorption (A) was determined by $A = 1 - R - T$, where R is the total reflectance measured from the glass side and T is the total transmittance through the back of solar cells ($T = 0$ for devices with gold electrode). R and T were measured using a Perkin Elmer LAMBDA 950 spectrometer equipped with an integrating sphere. PL spectra and PLQY measurements were carried out using a Horiba FluoroLog-3 spectrofluorometer in reflection geometry under ambient conditions. Integrated sphere was used for obtaining solution-phase PLQY values. The sample was excited using a 633 nm pulsed laser diode (<1 ns). The emission was passed through a 1000 nm blaze grating monochromator (iHR320) and collected by an infrared photomultiplier tube.

Measurement of TA: A regeneratively amplified Yb:KGW laser at a 5 kHz repetition rate (Light Conversion, Pharos) was used to generated ultrafast pulses at 1030 nm. The output of the laser passed through a beamsplitter, where one arm was sent to an optical parametric amplifier (Light Conversion, Orpheus) to generate photoexcitation (pump) pulses with a ≈350 fs duration, and the other arm was sent to a sapphire crystal to generate the near-infrared (NIR) continuum spectrum. The pump and probe pulses were then both sent into a commercial TA spectrometer (Ultrafast, Helios). The probe pulse was delayed relative to the pump pulse using a delay stage permitting delays up to 8 ns, and a chopper was used to block every other pump pulse. The signal after the sample was dispersed by a grating spectrograph (Ultrafast, Helios) and subsequently collected by a CCD camera. Lifetimes were fit using biexponential decays convoluted with a Gaussian to account for the instrument response function (IRF). TA spectral slices were fit as a sum of one or more Gaussian peaks with negative coefficients for bleaching signals and positive coefficients for photo induced absorption signals.

Fabrication of CQD Solar Cell Devices: ITO glass substrates were cleaned by soaking and sonicating sequentially in acetone, isopropyl alcohol, and deionized water. ZnO nanoparticles were synthesized as previously reported.[18,33] The ZnO nanoparticle solution was spin-coated onto the cleaned ITO glass two times at 3000 rpm for 30 s, and subsequently dual and lead halide-only passivated CQDs in a mixture of 90% BTA and 10% DMF (200 mg mL^{-1}) were spin-coated at 2600 rpm for 30 s. For the final device fabrication, two thin layers of EDT-treated CQDs (EDT-CQDs) were deposited, followed by gold deposition as a top metal electrode.

Supporting Information

Supporting Information is available from the Wiley Online Library or from the author.

Acknowledgements

Conflict of Interest

The authors declare no conflict of interest.

Keywords

[1] V. F. Puntes, K. M. Krishnan, A. P. Alivisatos, *Science* **2001**, *291*, 2115.

[2] M.-C. Daniel, D. Astruc, *Chem. Rev.* **2004**, *104*, 293.

[3] X. Wang, J. Zhuang, Q. Peng, Y. Li, *Nature* **2005**, *437*, 121.

[4] J. Park, J. Joo, S. G. Kwon, Y. Jang, T. Hyeon, *Angew. Chem., Int. Ed.* **2007**, *46*, 4630.

[5] Y. Kim, C. Lee, I. Shim, D. Wang, J. Cho, *Adv. Mater.* **2010**, *22*, 5140.

[6] M. J. Polking, M.-G. Han, A. Yourdkhani, V. Petkov, C. F. Kisielowski, V. V. Volkov, Y. Zhu, G. Caruntu, A. P. Alivisatos, R. Ramesh, *Nat. Mater.* **2012**, *11*, 700.

[7] T. R. Gordon, M. Cargnello, T. Paik, F. Mangolini, R. T. Weber, P. Fornasiero, C. B. Murray, *J. Am. Chem. Soc.* **2012**, *134*, 6751.

[8] T.-H. Yang, K. D. Gilroy, Y. Xia, *Chem. Sci.* **2017**, *8*, 6730.

[9] F. Fan, O. Voznyy, R. P. Sabatini, K. T. Bicanic, M. M. Adachi, J. R. McBride, K. R. Reid, Y.-S. Park, X. Li, A. Jain, R. Quintero-Bermudez, M. Saravanapavanantham, M. Liu, M. Korkusinski, P. Hawrylak, V. I. Klimov, S. J. Rosenthal, S. Hoogland, E. H. Sargent, *Nature* **2017**, *544*, 75.

[10] V. L. Colvin, M. C. Schlamp, A. P. Alivisatos, *Nature* **1994**, *370*, 354.

[11] W. K. Bae, J. Lim, D. Lee, M. Park, H. Lee, J. Kwak, K. Char, C. Lee, S. Lee, *Adv. Mater.* **2014**, *26*, 6387.

[12] X. Gong, Z. Yang, G. Walters, R. Comin, Z. Ning, E. Beauregard, V. Adinolfi, O. Voznyy, E. H. Sargent, *Nat. Photonics* **2016**, *10*, 253.

[13] G. Konstantatos, I. Howard, A. Fischer, S. Hoogland, J. Clifford, E. Klem, L. Levina, E. H. Sargent, *Nature* **2006**, *442*, 180.

[14] J.-S. Lee, M. V. Kovalenko, J. Huang, D. S. Chung, D. V. Talapin, *Nat. Nanotechnol.* **2011**, *6*, 348.

[15] M. A. Hines, G. D. Scholes, *Adv. Mater.* **2003**, *15*, 1844.

[16] S. A. McDonald, G. Konstantatos, S. Zhang, P. W. Cyr, E. J. D. Klem, L. Levina, E. H. Sargent, *Nat. Mater.* **2005**, *4*, 138.

[17] I. Gur, N. A. Fromer, M. L. Geier, A. P. Alivisatos, *Science* **2005**, *310*, 462.

[18] C.-H. M. Chuang, P. R. Brown, V. Bulović, M. G. Bawendi, *Nat. Mater.* **2014**, *13*, 796.

[19] A. H. Ip, A. Kiani, I. J. Kramer, O. Voznyy, H. F. Movahed, L. Levina, M. M. Adachi, S. Hoogland, E. H. Sargent, *ACS Nano* **2015**, *9*, 8833.

[20] A. Kiani, B. R. Sutherland, Y. Kim, O. Ouellette, L. Levina, G. Walters, C.-T. Dinh, M. Liu, O. Voznyy, X. Lan, A. J. Labelle, A. H. Ip, A. Proppe, G. H. Ahmed, O. F. Mohammed, S. Hoogland, E. H. Sargent, *Appl. Phys. Lett.* **2016**, *109*, 183105.

[21] O. Ouellette, N. Hossain, B. R. Sutherland, A. Kiani, F. P. García de Arquer, H. Tan, M. Chaker, S. Hoogland, E. H. Sargent, *ACS Energy Lett.* **2016**, *1*, 852.

[22] I. Moreels, B. Fritzinger, J. C. Martins, Z. Hens, *J. Am. Chem. Soc.* **2008**, *130*, 15081.

[23] A. Dong, X. Ye, J. Chen, Y. Kang, T. Gordon, J. M. Kikkawa, C. B. Murray, *J. Am. Chem. Soc.* **2011**, *133*, 998.

[24] J. Tang, K. W. Kemp, S. Hoogland, K. S. Jeong, H. Liu, L. Levina, M. Furukawa, X. Wang, R. Debnath, D. Cha, K. W. Chou, A. Fischer, A. Amassian, J. B. Asbury, E. H. Sargent, *Nat. Mater.* **2011**, *10*, 765.

[25] A. H. Ip, S. M. Thon, S. Hoogland, O. Voznyy, D. Zhitomirsky, R. Debnath, L. Levina, L. R. Rollny, G. H. Carey, A. Fischer, K. W. Kemp, I. J. Kramer, Z. Ning, A. J. Labelle, K. W. Chou, A. Amassian, E. H. Sargent, *Nat. Nanotechnol.* **2012**, *7*, 577.

[26] N. C. Anderson, M. P. Hendricks, J. J. Choi, J. S. Owen, *J. Am. Chem. Soc.* **2013**, *135*, 18536.

[27] H. Choi, J.-H. Ko, Y.-H. Kim, S. Jeong, *J. Am. Chem. Soc.* **2013**, *135*, 5278.

[28] Z. Ning, O. Voznyy, J. Pan, S. Hoogland, V. Adinolfi, J. Xu, M. Li, A. R. Kirmani, J. Sun, J. Minor, K. W. Kemp, H. Dong, L. Rollny, A. Labelle, G. Carey, B. Sutherland, I. Hill, A. Amassian, H. Liu, J. Tang, O. M. Bakr, E. H. Sargent, *Nat. Mater.* **2014**, *13*, 822.

[29] D. Zherebetskyy, M. Scheele, Y. Zhang, N. Bronstein, C. Thompson, D. Britt, M. Salmeron, A. P. Alivisatos, L.-W. Wang, *Science* **2014**, *344*, 1380.

[30] H. Zhang, J. Jang, W. Liu, D. V. Talapin, *ACS Nano* **2014**, *8*, 7359.

[31] R. W. Crisp, D. M. Kroupa, A. R. Marshall, E. M. Miller, J. Zhang, M. C. Beard, J. M. Luther, *Sci. Rep.* **2015**, *5*, 9945.

[32] X. Lan, O. Voznyy, A. Kiani, F. P. García de Arquer, A. S. Abbas, G.-H. Kim, M. Liu, Z. Yang, G. Walters, J. Xu, M. Yuan, Z. Ning, F. Fan, P. Kanjanaboos, I. Kramer, D. Zhitomirsky, P. Lee, A. Perelgut, S. Hoogland, E. H. Sargent, *Adv. Mater.* **2016**, *28*, 299.

[33] M. Liu, O. Voznyy, R. Sabatini, F. P. Garcia de Arquer, R. Munir, A. H. Balawi, X. Lan, F. Fan, G. Walters, A. R. Kirmani, S. Hoogland, F. Laquai, A. Amassian, E. H. Sargent, *Nat. Mater.* **2017**, *16*, 258.

[34] J. Xu, O. Voznyy, M. Liu, A. R. Kirmani, G. Walters, R. Munir, M. Abdelsamie, A. H. Proppe, A. Sarkar, F. P. García de Arquer, M. Wei, B. Sun, M. Liu, O. Ouellette, R. Quintero-Bermudez, J. Li, J. Fan, L. Quan, P. Todorovic, H. Tan, S. Hoogland, S. O. Kelley, M. Stefik, A. Amassian, E. H. Sargent, *Nat. Nanotechnol.* **2018**, *13*, 456.

[35] Y. Kim, K. Bicanic, H. Tan, O. Ouellette, B. R. Sutherland, F. P. García de Arquer, J. W. Jo, M. Liu, B. Sun, M. Liu, S. Hoogland, E. H. Sargent, *Nano Lett.* **2017**, *17*, 2349.

[36] H. Aqoma, M. A. Mubarok, W. T. Hadmojo, E.-H. Lee, T.-W. Kim, T. K. Ahn, S.-H. Oh, S.-Y. Jang, *Adv. Mater.* **2017**, *29*, 1605756.

[37] W. J. Baumgardner, K. Whitham, T. Hanrath, *Nano Lett.* **2013**, *13*, 3225.

[38] D. M. Balazs, D. N. Dirin, H.-H. Fang, L. Protesescu, G. H. ten Brink, B. J. Kooi, M. V. Kovalenko, M. A. Loi, *ACS Nano* **2015**, *9*, 11951.

[39] W. Walravens, J. D. Roo, E. Drijvers, S. ten Brinck, E. Solano, J. Dendooven, C. Detavernier, I. Infante, Zeger Hens, *ACS Nano* **2016**, *10*, 6861.

[40] J. J. Geuchies, C. van Overbeek, W. H. Evers, B. Goris, A. de Backer, A. P. Gantapara, F. T. Rabouw, J. Hilhorst, J. L. Peters, O. Konovalov, A. V. Petukhov, M. Dijkstra, L. D. A. Siebbeles, S. van Aert, S. Bals, D. Vanmaekelbergh. *Nat. Mater.* **2016**, *15*, 1248.

[41] A. Salis, B. W. Ninham, *Chem. Soc. Rev.* **2014**, *43*, 7358.

[42] G. Kresse, J. Hafner, *Phys. Rev. B* **1993**, *47*, 558.

[43] G. Kresse, J. Furthmüller, *Comput. Mater. Sci.* **1996**, *6*, 15.

[44] L. Köhler, G. Kresse, *Phys. Rev. B* **2004**, *70*, 165405.

[45] D. Pal, V. G. Stoleru, E. Towe, D. Firsov, *Jpn. J. Appl. Phys.* **2002**, *41*, 482.

[46] J. Gao, J. C. Johnson, *ACS Nano* **2012**, *6*, 3292.

[47] S. John, *Phys. Rev. Lett.* **1986**, *57*, 1777.

[48] D. Venkateshvaran, M. Nikolka, A. Sadhanala, V. Lemaur, M. Zelazny, M. Kepa, M. Hurhangee, A. J. Kronemeijer, V. Pecunia, I. Nasrallah, I. Romanov, K. Broch, I. McCulloch, D. Emin, Y. Olivier, J. Cornil, D. Beljonne, H. Sirringhaus, *Nature* **2014**, *515*, 384.

[49] B. Sun, O. Voznyy, H. Tan, P. Stadler, M. Liu, G. Wakters, A. H. Proppe, M. Liu, J. Fan, J. Li, M. Wei, J. Xu, Y. Kim, S. Hoogland, E. H. Sargent, *Adv. Mater.* **2017**, *29*, 170049.

[50] J. Choi, J. W. Jo, F. P. García de Arquer, Y.-B. Zhao, B. Sun, J. Kim, M.-J. Choi, S.-W. Baek, A. H. Proppe, A. Seifitokaldani, D.-H. Nam, P. Li, O. Ouellette, Y. Kim, O. Voznyy, S. Hoogland, S. O. Kelly, Z.-H. Lu, E. H. Sargent, *Adv. Mater.* **2018**, *30*, 1801720.

[51] Y. Kim, E. Yassitepe, O. Voznyy, R. Comin, G. Walters, X. Gong, P. Kanjanaboos, A. F. Nogueira, E. H. Sargent, *ACS Appl. Mater. Interfaces* **2015**, *7*, 25007.

[52] E. Yassitepe, Z. Yang, O. Voznyy, Y. Kim, G. Walters, J. A. Castañeda, P. Kanjanaboos, M. Yuan, X. Gong, F. Fan, J. Pan, S. Hoogland, R. Comin, O. M. Bakr, L. A. Padilha, A. F. Nogueira, E. H. Sargent, *Adv. Funct. Mater.* **2016**, *26*, 8757.